HAL
open science

Mining S-PLUS for Metal-poor Stars in the Milky Way

Vinicius M. Placco, Felipe Almeida-Fernandes, Anke Arentsen, Young Sun Lee, William Schoenell, Tiago Ribeiro, Antonio Kanaan

To cite this version:

Vinicius M. Placco, Felipe Almeida-Fernandes, Anke Arentsen, Young Sun Lee, William Schoenell, et al.. Mining S-PLUS for Metal-poor Stars in the Milky Way. The Astrophysical Journal Supplement Series, 2022, 262, 10.3847/1538-4365/ac7ab0 . insu-03763065

HAL Id: insu-03763065

https://insu.hal.science/insu-03763065v1

Submitted on 29 Aug 2022

HAL is a multi-disciplinary open access archive for the deposit and dissemination of scientific research documents, whether they are published or not. The documents may come from teaching and research institutions in France or abroad, or from public or private research centers.

L'archive ouverte pluridisciplinaire **HAL**, est destinée au dépôt et à la diffusion de documents scientifiques de niveau recherche, publiés ou non, émanant des établissements d'enseignement et de recherche français ou étrangers, des laboratoires publics ou privés.

Distributed under a Creative Commons Attribution 4.0 International License

The Astrophysical Journal Supplement Series, 262:8 (15pp), 2022 September https://doi.org/10.3847/1538-4365/ac7ab0
© 2022. The Author(s). Published by the American Astronomical Society.
OPEN ACCESS

Mining S-PLUS for Metal-poor Stars in the Milky Way

Vinicius M. Placco[1], Felipe Almeida-Fernandes[1,2], Anke Arentsen[3], Young Sun Lee[4], William Schoenell[5], Tiago Ribeiro[6], and Antonio Kanaan[7]
[1] NSF's NOIRLab, 950 N. Cherry Avenue, Tucson, AZ 85719, USA; vinicius.placco@noirlab.edu
[2] Departamento de Astronomia, Instituto de Astronomia, Geofísica e Ciências Atmosféricas da USP, Cidade Universitária, 05508-900, São Paulo, SP, Brazil
[3] Université de Strasbourg, CNRS, Observatoire Astronomique de Strasbourg, UMR 7550, F-67000 Strasbourg, France
[4] Department of Astronomy and Space Science, Chungnam National University, Daejeon 34134, Republic of Korea
[5] GMTO Corporation, 465 N. Halstead Street, Suite 250, Pasadena, CA 91107, USA
[6] Rubin Observatory Project Office, 950 N. Cherry Avenue, Tucson, AZ 85719, USA
[7] Departamento de Física, Universidade Federal de Santa Catarina, Florianópolis, SC 88040-900, Brazil
Received 2022 June 1; revised 2022 June 14; accepted 2022 June 16; published 2022 August 19

Abstract

This work presents the medium-resolution ($R \sim 1500$) spectroscopic follow-up of 522 low-metallicity star candidates from the Southern Photometric Local Universe Survey (S-PLUS). The objects were selected from narrowband photometry, taking advantage of the metallicity-sensitive S-PLUS colors. The follow-up observations were conducted with the Blanco and Gemini South telescopes, using the COSMOS and GMOS spectrographs, respectively. The stellar atmospheric parameters ($T_{\rm eff}$, log g, and [Fe/H]), as well as carbon and α-element abundances, were calculated for the program stars in order to assess the efficacy of the color selection. Results show that 92^{+2}_{-3}% of the observed stars have [Fe/H] $\leqslant -1.0$, 83^{+3}_{-3}% have [Fe/H] $\leqslant -2.0$, and 15^{+3}_{-3}% have [Fe/H] $\leqslant -3.0$, including two ultra metal-poor stars ([Fe/H] $\leqslant -4.0$). The 80th percentile for the metallicity cumulative distribution function of the observed sample is [Fe/H] $= -2.04$. The sample also includes 68 carbon-enhanced metal-poor stars. Based on the calculated metallicities, further S-PLUS color cuts are proposed, which can increase the fractions of stars with [Fe/H] $\leqslant -1.0$ and $\leqslant -2.0$ to 98% and 88%, respectively. Such high success rates enable targeted high-resolution spectroscopic follow-up efforts, as well as provide selection criteria for fiber-fed multiplex spectroscopic surveys.

Unified Astronomy Thesaurus concepts: Narrow band photometry (1088); Metallicity (1031); Stellar atmospheres (1584); Chemical abundances (224)

Supporting material: machine-readable tables

1. Introduction

There is a wealth of information contained in the colors of stars (Allende Prieto 2016), which are simply the difference in integrated fluxes on two given photometric bandpasses. The first determinations of effective temperatures from photometry date back to the early 20th century (Greaves et al. 1929) and since then extensive work has been conducted to characterize and calibrate temperature scales in optical (Bessell 1979) and near-infrared (Alonso et al. 1996, 1999; Casagrande et al. 2010) systems, just to mention a few. The same applies to estimating the metallicity ([Fe/H][8]) of stellar sources from photometry. Many studies in the literature relied on the calibration of the ultraviolet excess for stellar sources, which is heavily dependent on the metallicity (Wallerstein 1964; Schuster & Nissen 1989; Bonifacio et al. 2000), but there are others that take advantage of infrared colors, depending on the stellar population (e.g., cold brown dwarfs—Leggett et al. 2010).

More recently, large-scale surveys have taken these photometric parameter determination strategies to the next level by building databases with millions of spectroscopically observed objects. Two such examples are the Sloan Digital Sky Survey (SDSS; York et al. 2000) in the Northern Hemisphere and the SkyMapper Sky Survey (SMSS; Wolf et al. 2018) in the Southern Hemisphere. Both of these surveys conducted separate subsurveys aiming to perform medium-resolution ($R \sim 1500$) spectroscopic follow-up of stars in the the Milky Way: the Sloan Extension for Galactic Understanding and Exploration (SEGUE-1; Yanny et al. 2009) and SEGUE-2 (Rockosi et al. 2022), and the AAOmega Evolution of Galactic Structure (AEGIS; Keller et al. 2007; Yoon et al. 2018, among others). These not only served as the basis for a number of statistical studies of stellar populations in the Milky Way (Ivezić et al. 2012), but also as prime data sets for high-resolution spectroscopic follow-up and calibration of photometric parameter determinations.

The SDSS makes use of the Sloan Photometric System, which comprises five colors ($u'/g'/r'/i'/z'$) that cover the region between 3000 Å and 11000 Å into five essentially nonoverlapping passbands (Fukugita et al. 1996). Ivezić et al. (2008) were able to determine temperatures (with typical uncertainties of ~100 K) and metallicities (with uncertainties of 0.2 dex or better for $-2.0 \leqslant$ [Fe/H] $\leqslant -0.5$) for over 2 million F/G stars in the Milky Way. One of the limitations on the low-metallicity end is due to the broadness of the u filter, which loses its metallicity sensitivity, hampering efforts to extend the determinations to [Fe/H] $\leqslant -2.5$. In two follow-up studies from the work of Ivezić et al. (2008), An et al. (2013) and An et al. (2015) redetermined the photometric metallicities and the metallicity distribution functions (MDFs) in the Galactic halo from SDSS photometry. These efforts relied on improved photometry from the Stripe 82 region of SDSS and were able to

[8] $[A/B] = \log(N_A/N_B)_\star - \log(N_A/N_B)_\odot$, where N is the number density of atoms of a given element in the star ($\star$) and the Sun ($\odot$), respectively.

Original content from this work may be used under the terms of the Creative Commons Attribution 4.0 licence. Any further distribution of this work must maintain attribution to the author(s) and the title of the work, journal citation and DOI.

increase the metallicity range of the photometric estimates down to [Fe/H] ~ -2.5.

The SkyMapper filter set design was optimized for stellar astrophysics, in particular the study of stellar populations in the Milky Way (Keller et al. 2007). It is composed of six filters: $u/v/g/r/i/z$ (Bessell et al. 2011). The u ($\lambda_{\rm cen} = 349$ nm) and v ($\lambda_{\rm cen} = 384$ nm) filters are a two-filter version of the SDSS u', providing additional photometric sensitivity. The SkyMapper Data Release 1 (DR1; Wolf et al. 2018) has been extensively used to determine photometric stellar atmospheric parameters and select low-metallicity stars for spectroscopic follow-up. Casagrande et al. (2019), using the SkyMapper DR1, were able to determine temperatures and metallicities with uncertainties better than $\sim$100 K and $\sim$0.2 dex for [Fe/H] $\geqslant -2.0$, respectively. A similar study by Huang et al. (2019), limited to red giant stars, was able to reach slightly lower uncertainties ($\sim$80 K and $\sim$0.18 dex), however, with the parameter space still limited to [Fe/H] $\geqslant -2.0$, with only a few objects with metallicities below this threshold. Chiti et al. (2021a) extended the low-metallicity limit to [Fe/H] < -2.5 with $\sigma \sim 0.31$ dex, with the goal of constructing the photometric MDF of the Milky Way (Chiti et al. 2021b). In terms of spectroscopic follow-up, Da Costa et al. (2019) present 2618 candidates selected to have photometric [Fe/H] < -2.0 from their metallicity-sensitive diagram. Results show that over 40% of the observed stars have [Fe/H] $\leqslant -2.75$.

The Pristine Survey (Starkenburg et al. 2017) has been successfully using narrowband photometry on the metallicity sensitive Ca II H and K absorption features (in addition to SDSS broadband g and i) to search for low-metallicity stars in the galaxy from the Northern Hemisphere. The $\sim$100 Å wide narrowband filter has a larger predictive power than the broadband counterparts of SDSS and SkyMapper and is able to successfully predict metallicities in the [Fe/H] ~ -3.0 regime (Youakim et al. 2017). The results of a 3 yr medium-resolution spectroscopic follow-up campaign show that $\sim$70% of the 1007 stars observed have [Fe/H] < -2.0 and $\sim$9% have [Fe/H] < -3.0 (Aguado et al. 2019).[9]

The Javalambre Photometric Local Universe Survey (J-PLUS; Cenarro et al. 2019) and the Southern Photometric Local Universe Survey (S-PLUS; Mendes de Oliveira et al. 2019) have a unique 12 broad- and narrowband filter set, consisting of four SDSS (g, r, i, z), one modified SDSS u, and seven narrowband filters. The narrowband filters were designed to probe very specific regions in the optical wavelength regime and accommodate a wide variety of science cases, from high-precision photometric redshifts (Molino et al. 2020) to the identification of low-metallicity stars in the Galactic halo (Galarza et al. 2022). The names and key absorption features sampled by the narrowband filters are $J0378$—[O II], $J0395$—Ca II H+K, $J0410$—Hδ, $J0430$—G band, $J0515$—Mg b triplet, $J0660$—Hα, and $J0861$—Ca triplet. It is worth pointing out that the $J0395$ filter shares a similar central wavelength and width as the Pristine narrowband filter. However, J-PLUS and S-PLUS have the advantage of also performing narrowband photometry in the Mg b triplet ($J0515$) and Ca ($J0861$) triplet regions, which are also useful for metallicity and surface gravity determinations (Majewski et al. 2000). Whitten et al. (2019) used J-PLUS photometry to predict $T_{\rm eff}$ and [Fe/H] using artificial neural networks and reached uncertainties of $\sim$91 K and $\sim$0.25 dex for stars in the $-3.0 \lesssim$ [Fe/H] $\leqslant -0.5$. In a follow-up study using S-PLUS, Whitten et al. (2021) were able to estimate the first photometric carbon abundances for a sample of over 50,000 stars, with uncertainties better than $\sim$0.35 dex. Finally, Galarza et al. (2022) used J-PLUS photometry to predict stellar atmospheric parameters from machine-learning techniques, reaching a success rate of 64% in identifying stars with [Fe/H] < -2.5, confirmed by medium-resolution spectroscopic follow-up.

The possibility of accurately determining stellar atmospheric parameters and chemical abundances for large data sets drawn from photometry, and especially for a wide range of metallicities, is fundamental in the context of studying low-metallicity stars. Very metal-poor (VMP, [Fe/H] < -2.0; Beers & Christlieb 2005) stars are the "local" observational probes that allow astronomers to address questions at cosmological scales (Bromm & Larson 2004). The research that was once limited to individual stars (Carney & Peterson 1981) has been expanded to much larger samples, allowing the investigation of relations such as the carbon-enhancement observed in metal-poor stars (Lucatello et al. 2006; Aoki et al. 2007), the possible origins of the subclasses within this group (Masseron et al. 2010), their role in the chemical evolution of the early universe (Woosley & Weaver 1995; Heger & Woosley 2002; Meynet et al. 2006; Norris et al. 2013; Frebel & Norris 2015), and the connection between the Galactic halo and low-mass dwarf galaxies accreted within the context of hierarchical assembly (Yuan et al. 2020; Limberg et al. 2021a; Shank et al. 2022, among others). Growing statistics on VMP stars narrow error bars and broadens our understanding of the early stages of the chemical evolution of the universe.

This article reports on the medium-resolution ($R \sim 1500$) spectroscopic follow-up of low-metallicity star candidates selected from the S-PLUS Data Release 3 (DR3). The main goal is to assess whether the metallicity-sensitive S-PLUS colors are effective in selecting metal-poor stars for spectroscopic follow-up. Section 2 describes the medium-resolution spectroscopic observations, followed by the estimates of the stellar atmospheric parameters and abundances in Section 3. In Section 4 we analyze the sensitivity of the narrowband photometry to the stellar parameters, the effectiveness of the S-PLUS color selection for low-metallicity stars, the distribution of carbon and α-element abundances, and further improvements in the color selection. Our conclusions and prospects for future work are provided in Section 5.

2. Target Selection and Observations

2.1. The S-PLUS Data Release 3

For this work, the S-PLUS Data Release 3 (DR3; M. L. Buzzo et al. 2022, in preparation) was used. The data structure in this data release, as well as the photometric extraction and calibration process, are the same as the S-PLUS Data Release 2 (DR2; Almeida-Fernandes et al. 2022). The only difference is the addition of observations in the South Galactic Hemisphere for DR3. At the time the candidates for this work were selected, the catalogs were only available internally to the collaboration and are now publicly available through the `S-PLUS Cloud`[10] service.

The first step in the data selection was to apply a series of restrictions in the DR3 database, which originally contained

[9] The Pristine Survey has individual photometric metallicities to compare to the spectroscopic determinations. For the work of Aguado et al. (2019), 23% of the stars with photometric [Fe/H] < -3.0 also have spectroscopic [Fe/H] < -3.0.

[10] https://splus.cloud/

13,416,120 sources, mostly related to the quality of the photometry, probability of being a stellar source, and a color range suitable to study low-metallicity stars. Then, metal-poor star candidates were chosen for the medium-resolution spectroscopic campaign, based on their location on a metallicity-dependent color–color diagram, as described below. The following restrictions were applied to the DR3 database:

1. `CLASS_STAR` $\geqslant 0.95$: sources having a high probability of being a star;
2. `gSDSS` $\leqslant$ `17.5`: brightness limit for spectroscopic follow-up within reasonable exposure times;
3. `nDet_magPStotal` = `12`: only sources with all 12 magnitudes measured;
4. `(gSDSS-iSDSS)` $\in$ `[0.2:1.6]`: color window to remove possible contamination from white dwarfs and A-type stars on the blue end and objects cooler than $T_{\rm eff}\sim$4000 K on the red end (see Figure 3 in Yanny et al. 2009);
5. `(J0410-J0861)` $\in$ `[0.3:3.5]`: same as above using a narrowband color;
6. `Total`: 820,829 stars.

The S-PLUS magnitudes used throughout this work are the 3″ aperture corrected values, labeled `PStotal`. The left panel of Figure 1 shows the density of the selected stars in a color–color diagram. The color `(J0395-J0660)-2×(g-i)` was chosen based on the work of Starkenburg et al. (2017) for the Pristine Survey, which is proven to have a strong [Fe/H] dependency. The g filter was replaced with `J0660` as a temperature-sensitive feature and `-2×(g-i)` was used to reshape the color–color diagram. On the x-axis, both Starkenburg et al. (2017) and Da Costa et al. (2019) employ the $(g-i)_0$ color. Due to the dependency of the Ca II K line strength with temperature, there is a color range, roughly $(g-i)_0 \lesssim 0.3$, where the metallicity-dependent color difference between a star with [Fe/H] = −2.0 and −4.0 becomes smaller than the typical uncertainties in the photometry. In an attempt to address this degeneracy, this work employs the `(J0395-J0410)-(J0660-J0861)` combination, that uses the filters centered on Hδ and Hα and provides better temperature sensitivity. This temperature-dependent metallicity color index should increase the success rate of finding metal-poor stars. The transmission curves for the six S-PLUS filters used in this selection are shown in the top right panel of Figure 1.

The catalog generated from the S-PLUS DR3 selection above was crossmatched with the SDSS/SEGUE spectroscopic database. From that crossmatch, sources with `CLASS==QSO`, $\sigma_{\rm Teff} > 200$K, and `S/N` $<$ `20` were excluded. The bottom right panel of Figure 1 shows a section of the color–color diagram, with each 0.01 × 0.01 bin colored by its average [Fe/H] value from the spectroscopic data. Also shown in each bin are the number of stars used to calculate the average. The metallicity dependency is very evident in both axes and allows for an improved selection of potential metal-poor stars for spectroscopic follow-up.

Figure 2 further explores this color space. Each panel shows a different metallicity regime, color-coded by the fraction of stars in each 0.05 × 0.05 bin. The number of stars in each bin is also shown. As an example, the bin centered on `(0.0,-0.1)` has 1 star with [Fe/H] > -1.0 (∼2%), 19 stars with $-2.0 <$ [Fe/H] $\leqslant -1.0$ (∼46%), and 21 stars with [Fe/H] $\leqslant -2.0$ (∼52%). For the spectroscopic follow-up, from the right panel, a cut was made where most bins have at least a 50% fraction of [Fe/H] $\leqslant -2.0$ star. Limits were also placed on the blue end of each color, to avoid sources with potentially spurious colors. The final color window for the selection of targets for the spectroscopic follow-up was defined as `(J0395-J0410)-(J0660-J0861)` $\in$`[-0.30:0.15]` and `(J0395-J0660)-2×(g-i)` $\in$`[-0.60:-0.15]` (see the red box in the left panel of Figure 1). Within this window, which contains 11,118 stars from S-PLUS DR3, targets were chosen based on their brightness and observability at a given telescope, as well as giving preference to objects located in the bottom left part of the selection window. Further details are provided in the next section.

2.2. Medium-resolution Spectroscopy

The spectroscopic follow-up campaign was conducted in semesters 2019A, 2019B, 2020A, 2021A, and 2022A. Data were collected for 522 metal-poor star candidates, selected from their S-PLUS photometry, described above. The stars were observed with two different telescope/instrument setups: Blanco/COSMOS and Gemini South/GMOS-S.

Prior to the start of the observing campaigns in late 2018, the S-PLUS candidate list was crossmatched with the `SIMBAD` Astronomical Database[11] and stars with previously determined stellar parameters were excluded. After the follow-up observations were concluded, another crossmatch was conducted for the 522 observed targets, and four stars were found to have recent stellar parameter determinations: 2MASSJ03145801−3236489 and 2MASSJ04441395−3356317 (Steinmetz et al. 2020), 2MASSJ11120172−2212075 (Cordoni et al. 2021), and 2MASSJ13103235−1257092 (Placco et al. 2019). The published parameters all agree within 2σ with the values determined in this work (see Section 3 for details).

The distribution (in Galactic coordinates) of the observed stars is shown in the top panel of Figure 3, color-coded by telescope. The point size is proportional to the g magnitude of each target. The dust map traces the Galactic plane and was constructed from the Schlegel et al. (1998) reddening values. Also shown (gray solid line) is the celestial equator. The apparent grouping of the stars is due to the S-PLUS observing strategy, which started with the `STRIPE82` (equatorial) region (DR1), then moving toward halo fields at lower southern declinations (DR2 and DR3). Note that most of the faint targets were observed with the Gemini telescope, due to its larger aperture. Table 1 lists the name, coordinates, and observing details for each star. The bottom panels of Figure 3 show the magnitude distribution of the observed targets in all the 12 S-PLUS filters. Each panel displays the transmission curve for the filters with their central wavelength (in Å). Table 2 lists all the magnitude values (and errors) for the observed stars, taken from the S-PLUS DR3 catalog.

For consistency in the spectroscopic observations, grating/slit combinations were chosen to yield a resolving power $R \sim 1200 - 1800$, and exposure times were set to reach a signal-to-noise ratio (S/N) of at least S/N ∼ 30 per pixel at the Ca II K line (3933.3 Å). Calibration frames included arc-lamp exposures, bias frames, and quartz flats. Specific details of each instrument and data reduction are given below.

CTIO Blanco Telescope. A total of 384 stars were observed with the Víctor M. Blanco 4-meter Telescope, located at the

[11] http://simbad.cds.unistra.fr/simbad/

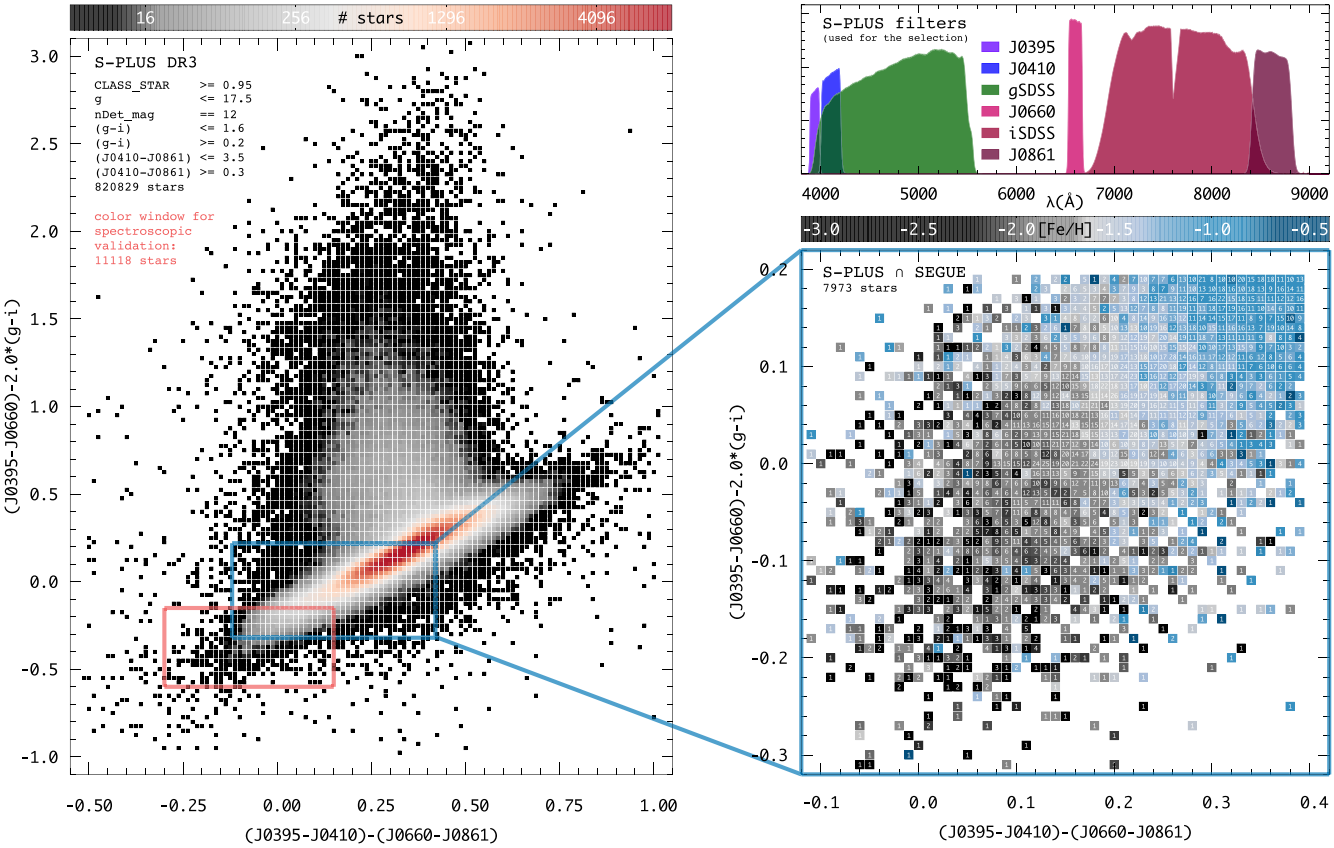

Figure 1. Left panel: stellar density for the selected S-PLUS DR3 sample in a color–color diagram. The red box outlines the color window for the spectroscopic follow-up (see the text for details). The inset (bottom right panel) shows the crossmatch with the SDSS/SEGUE spectroscopic database, color-coded by the average metallicity in each bin. The number of stars in each bin is also shown. Top right panel: S-PLUS transmission curves for the six narrowband and broadband filters used in this selection.

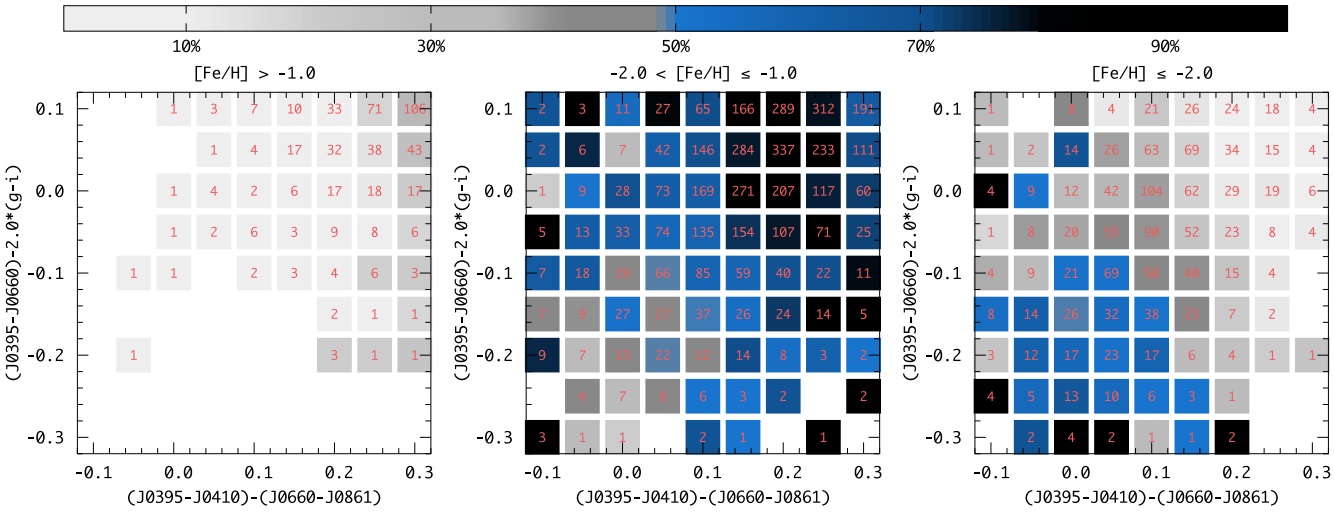

Figure 2. Color–color diagram for three different [Fe/H] regimes. The bins in each panel are color-coded by the fraction of stars with an average metallicity in a given range. The number of stars in each bin is also shown.

Cerro Tololo Inter-American Observatory, using the Cerro Tololo Ohio State Multi-Object Spectrograph (COSMOS; Martini et al. 2014) instrument. Observations were conducted in remote visitor mode in 2019 October, 2020 December, 2021 January, and 2022 April (2019B-0069, 2020A-0032, and 2022A-210002). The exposure times ranged from 90 to 1800 s, with a total of 57.96 hr on target. The setup included a 600 l mm^{-1} grating (blue setting) and a 1″.5 slit, resulting in a wavelength coverage in the range [3600:6300] Å at resolving power $R \sim 1800$. All tasks related to spectral reduction, extraction, and wavelength calibration were performed using standard IRAF[12] packages.

[12] https://iraf-community.github.io/

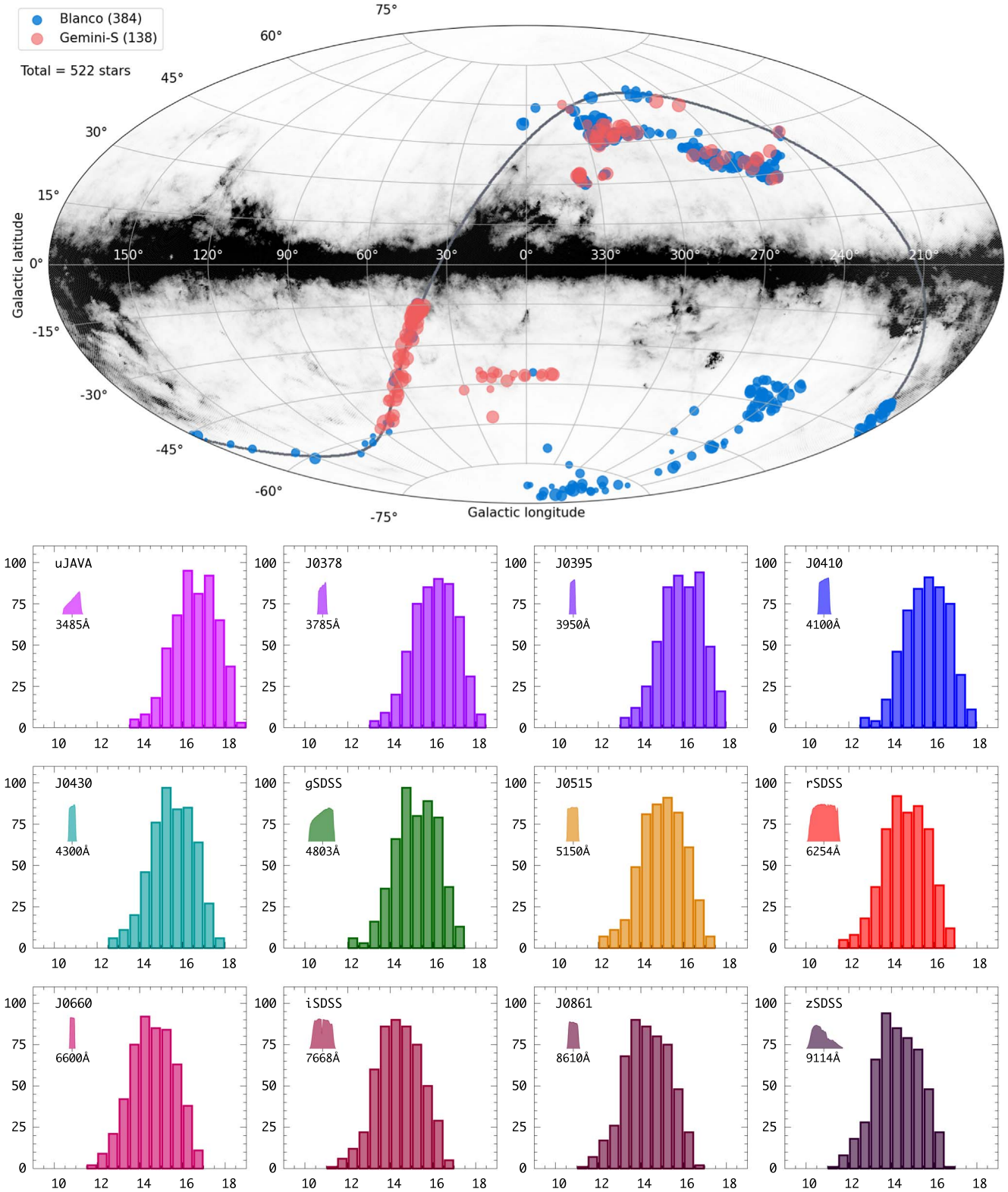

Figure 3. Top: Galactic coordinates for the stars observed in this work, color coded by telescope. The point size is proportional to the g magnitude. The gray line traces the celestial equator. The dust map uses reddening values from Schlegel et al. (1998). Bottom: magnitude distribution of the observed stars in the 12-filter system of S-PLUS. Each panel also shows the name, transmission curve, and central wavelength (in angstroms) for the filters.

Gemini South Telescope. A total of 138 stars were observed with the 8.1 m Gemini South telescope and the Gemini Multi-Object Spectrographs (GMOS; Davies et al. 1997; Gimeno et al. 2016) instrument. Observations were conducted in the "Poor Weather" queue mode in 2019 April–June, 2021 June–July, and 2022 April–June (GS-2019A-Q-408, GS-2021A-Q-419, and GS-2022A-Q-406). The exposure times ranged from 210 to 1800 s, with a total of 45.84 hr on target. The B600 1 mm^{-1} grating (G5323) and a 1″.5 slit were used with a 2×2 binning, resulting in a wavelength coverage in the range

Table 1
Observing Details

Star Name (SPLUS)	Star Name (2MASS)	α (J2000)	δ (J2000)	l (deg)	b (deg)	Date (UTC)	Telescope	Instrument	Proposal ID	Exp. (s)
J000445.50+010117.0	J00044550+0101170	00:04:45.60	+01:01:15.6	99.307	−59.692	2020-12-26	Blanco	COSMOS	2020A-0032	360
J001736.44+000921.7	J00173643+0009215	00:17:36.48	+00:09:21.6	104.962	−61.530	2020-12-27	Blanco	COSMOS	2020A-0032	360
J002554.41−305032.0	J00255442−3050320	00:25:54.48	−30:50:31.2	357.784	−83.297	2020-12-27	Blanco	COSMOS	2020A-0032	360
J002712.10−313352.1	J00271209−3133515	00:27:12.00	−31:33:50.4	351.455	−83.105	2020-12-25	Blanco	COSMOS	2020A-0032	360
J002712.43+010037.0	J00271240+0100377	00:27:12.48	+01:00:36.0	110.255	−61.264	2020-12-26	Blanco	COSMOS	2020A-0032	360
J003555.86−420431.0	J00355591−4204306	00:35:55.92	−42:04:30.0	313.910	−74.721	2021-1-11	Blanco	COSMOS	2020A-0032	180
J005037.10−315413.2	J00503713−3154131	00:50:37.20	−31:54:14.4	305.016	−85.221	2020-12-28	Blanco	COSMOS	2020A-0032	540
J005037.17−340816.7	J00503717−3408167	00:50:37.20	−34:08:16.8	304.318	−82.988	2021-1-11	Blanco	COSMOS	2020A-0032	90
J005208.98−004609.9	J00520900−0046092	00:52:08.88	−00:46:08.4	123.332	−63.640	2019-10-17	Blanco	COSMOS	2019B-0069	600
J005428.84−300101.7	J00542886−3001012	00:54:28.80	−30:01:01.2	290.094	−87.035	2020-12-25	Blanco	COSMOS	2020A-0032	480

(This table is available in its entirety in machine-readable form.)

Table 2
S-PLUS Photometry

Star Name	uJAVA	σ	J0378	σ	J0395	σ	J0410	σ	J0430	σ	gSDSS	σ	J0515	σ	rSDSS	σ	J0660	σ	iSDSS	σ	J0861	σ	zSDSS	σ
J000445.50 +010117.0	15.150	0.004	14.629	0.004	14.530	0.006	14.283	0.004	14.195	0.004	13.862	0.001	13.659	0.003	13.313	0.001	13.275	0.001	13.093	0.001	13.014	0.002	12.978	0.001
J001736.44 +000921.7	15.996	0.006	15.434	0.006	15.321	0.008	14.994	0.006	14.889	0.005	14.523	0.002	14.284	0.004	13.908	0.001	13.841	0.002	13.638	0.001	13.529	0.002	13.498	0.001
J002554.41 −305032.0	15.891	0.008	15.341	0.008	15.168	0.011	14.946	0.009	14.803	0.008	14.530	0.003	14.354	0.005	14.043	0.002	13.984	0.002	13.829	0.002	13.770	0.003	13.729	0.002
J002712.10 −313352.1	15.082	0.005	14.655	0.006	14.498	0.008	14.198	0.006	14.090	0.006	13.845	0.002	13.609	0.003	13.349	0.001	13.299	0.001	13.123	0.001	13.042	0.002	13.039	0.001
J002712.43 +010037.0	15.296	0.005	14.837	0.005	14.711	0.007	14.485	0.005	14.385	0.005	14.144	0.002	13.934	0.003	13.658	0.001	13.622	0.001	13.464	0.001	13.394	0.002	13.370	0.001
J003555.86 −420431.0	15.575	0.005	15.142	0.006	14.967	0.008	14.758	0.006	14.668	0.006	14.480	0.002	14.280	0.004	14.033	0.002	14.046	0.002	13.883	0.002	13.835	0.003	13.808	0.002
J005037.10 −315413.2	16.459	0.009	15.981	0.010	15.805	0.013	15.606	0.010	15.500	0.010	15.251	0.004	15.059	0.007	14.790	0.002	14.743	0.003	14.586	0.002	14.533	0.004	14.501	0.003
J005037.17 −340816.7	15.724	0.006	15.058	0.005	14.892	0.008	14.436	0.005	14.190	0.005	13.745	0.002	13.487	0.003	12.997	0.001	12.926	0.001	12.658	0.001	12.550	0.001	12.493	0.001
J005208.98 −004609.9	15.402	0.004	14.967	0.005	14.787	0.006	14.626	0.005	14.528	0.004	14.316	0.002	14.129	0.003	13.881	0.001	13.853	0.002	13.723	0.001	13.660	0.002	13.639	0.002
J005428.84 −300101.7	15.796	0.006	15.352	0.007	15.218	0.011	15.002	0.007	14.886	0.006	14.640	0.003	14.496	0.004	14.184	0.002	14.152	0.002	13.980	0.002	13.922	0.003	13.895	0.002

(This table is available in its entirety in machine-readable form.)

Table 3
Stellar Parameters and Abundances from the n-SSPP

Star Name (SPLUS)	$T_{\rm eff}$ (K)	log g (cgs)	[Fe/H]	[C/Fe]	Δ[C/Fe][a]	$[{\rm C/Fe}]_{\rm cor}$[b]	$A({\rm C})_{\rm cor}$[c]	[α/Fe]
J000445.50+010117.0	5227	2.56	−2.37	+0.85	+0.02	+0.87	+6.93	+0.30
J001736.44+000921.7	4993	2.19	−2.63	+0.61	+0.01	+0.62	+6.42	+0.20
J002554.41−305032.0	5186	1.72	−2.21	+0.05	+0.35	+0.40	+6.62	+0.31
J002712.10−313352.1	5257	2.74	−2.27	+0.24	+0.01	+0.25	+6.41	+0.12
J002712.43+010037.0	5394	3.41	−2.29	+0.21	0.00	+0.21	+6.35	+0.53
J003555.86−420431.0	5645	3.38	−2.53	+0.51	0.00	+0.51	+6.41	+0.31
J005037.10−315413.2	5384	3.06	−2.32	+0.26	+0.01	+0.27	+6.38	+0.15
J005037.17−340816.7	4434	0.88	−2.71	⋯	⋯	⋯	⋯	+0.47
J005208.98−004609.9	5556	2.85	−2.99	+0.58	+0.01	+0.59	+6.03	+0.35
J005428.84−300101.7	5497	3.53	−2.05	+0.14	0.00	+0.14	+6.52	+0.01

Notes.
[a] Carbon correction from Placco et al. (2014).
[b] Corrected carbon-to-iron ratio.
[c] Corrected absolute carbon abundance.

(This table is available in its entirety in machine-readable form.)

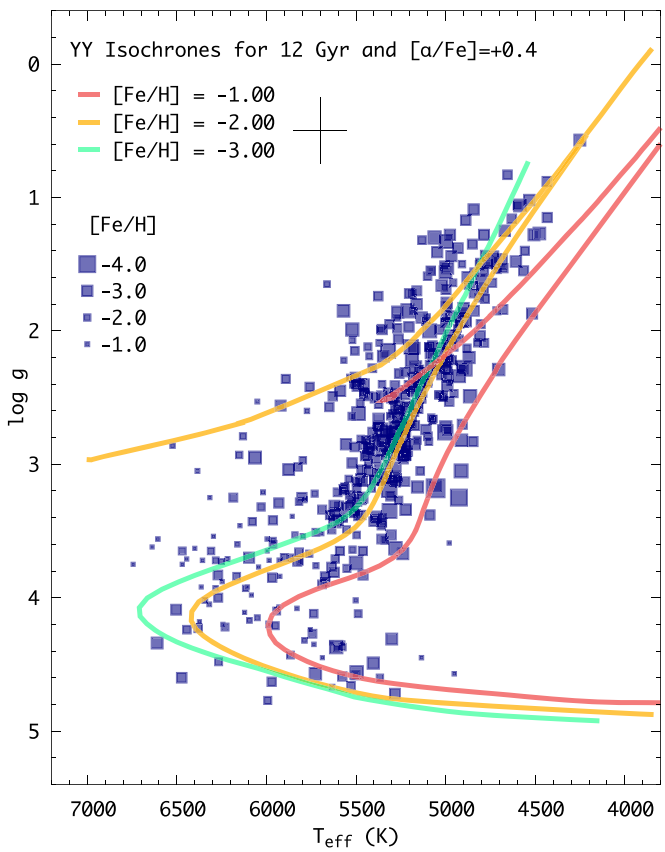

Figure 4. Surface gravity vs. $T_{\rm eff}$ diagram for the program stars, using the parameters calculated by the n-SSPP, listed in Table 3. Typical uncertainties are shown for reference. The point size is inversely proportional to the metallicity. Also shown are the YY Isochrones (12 Gyr, 0.8 $M_{\odot}$, [α/Fe] = +0.4; Demarque et al. 2004) for [Fe/H] = −1.0, −2.0, and −3.0, and horizontal-branch tracks from Dotter et al. (2008).

[3200:5800] Å at resolving power $R \sim 1200$. The complete data reduction was performed using the DRAGONS[13] software package (Labrie et al. 2019).

[13] https://github.com/GeminiDRSoftware/DRAGONS

3. Stellar Parameters and Chemical Abundances

The determinations of stellar atmospheric parameters ($T_{\rm eff}$, log g, and [Fe/H]), carbonicity ([C/Fe]), and α-to-iron ratios ([α/Fe]) for the stars observed as part of spectroscopic follow-up were made using the n-SSPP (Beers et al. 2014, 2017), a modified version of the SEGUE Stellar Parameter Pipeline (SSPP; Lee et al. 2008a, 2008b, 2011, 2013). The code uses photometric and spectroscopic information to calculate the atmospheric parameters based on several different methods, including calibrations with spectral line indices (from the Ca II H and K lines for [Fe/H]), photometric $T_{\rm eff}$ predictions, and synthetic spectra matching. Further details can be found in Placco et al. (2018).

The [C/Fe] and [α/Fe] are estimated from the strength of the CH G-band molecular feature at ∼4300 Å and the Mg I triplet at 5150–5200 Å, respectively. For the spectral fitting, the n-SSPP uses a grid of synthetic spectra generated with the MARCS model atmospheres (Gustafsson et al. 2008), CH line lists from Masseron et al. (2014), and the TURBOSPECTRUM code (Plez 2012), for the [C/Fe] determination. For [α/Fe], a grid of synthetic spectra are created with the Kurucz model atmospheres[14] and line lists,[15] which is an updated version from Lee et al. (2011). The high-resolution synthetic spectra have their resolution degraded to match that of the observed data. The n-SSPP was able to estimate $T_{\rm eff}$, log g, and [Fe/H] for all the 522 stars observed as part of this work. The [C/Fe] and [α/Fe] abundance ratios were estimated for 455[16] and 483 stars, respectively.

The adopted stellar parameters and their uncertainties are calculated as the biweight average of the individual accepted estimates and a robust estimate of the scatter (see details in Lee et al. 2008a). For the [C/Fe] and [α/Fe] abundance ratios, the values are determined by minimizing the distance between the target and synthetic fluxes, using a reduced χ^2 statistical criterion. Uncertainties are estimated by the square root of

[14] http://kurucz.harvard.edu/grids.html
[15] http://kurucz.harvard.edu/LINELISTS
[16] Most stars without carbon abundance determinations were observed with CTIO/Blanco. There was an artifact at the exact same position as the CH band head that affected some of the spectra and prevented reliable spectral fits by the n-SSPP.

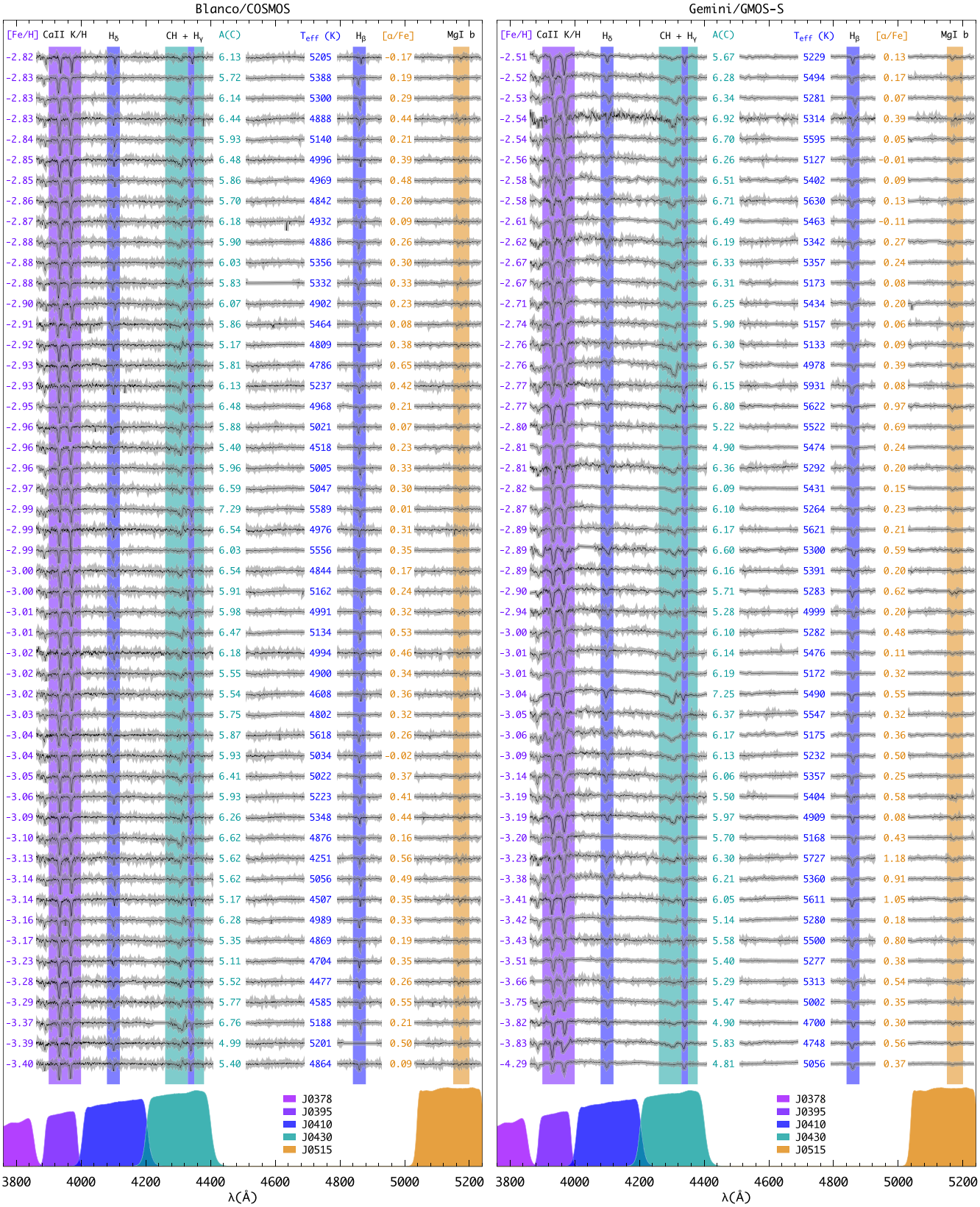

Figure 5. Example spectra for 100 program stars observed with Blanco (left panel) and Gemini South (right panel), sorted by decreasing metallicity. The shaded areas highlight absorption features of interest for the determination of the stellar parameters and chemical abundances (see the text for details). Also shown are the values calculated by the n-SSPP, as well as the S-PLUS filters that probe such features, with the exception of Hγ and Hβ.

diagonal elements of the resulting covariance matrix obtained during the χ^2 minimization (Lee et al. 2013). In addition, noise-injected synthetic spectra are used to derive the uncertainty as a function of S/N (see Lee et al. 2011, 2013 for details), by matching the S/N of the observed data. The average uncertainties for the observed sample are 70 K for $T_{\rm eff}$ ($\sigma T_{\rm eff} \in$ [40:175]),

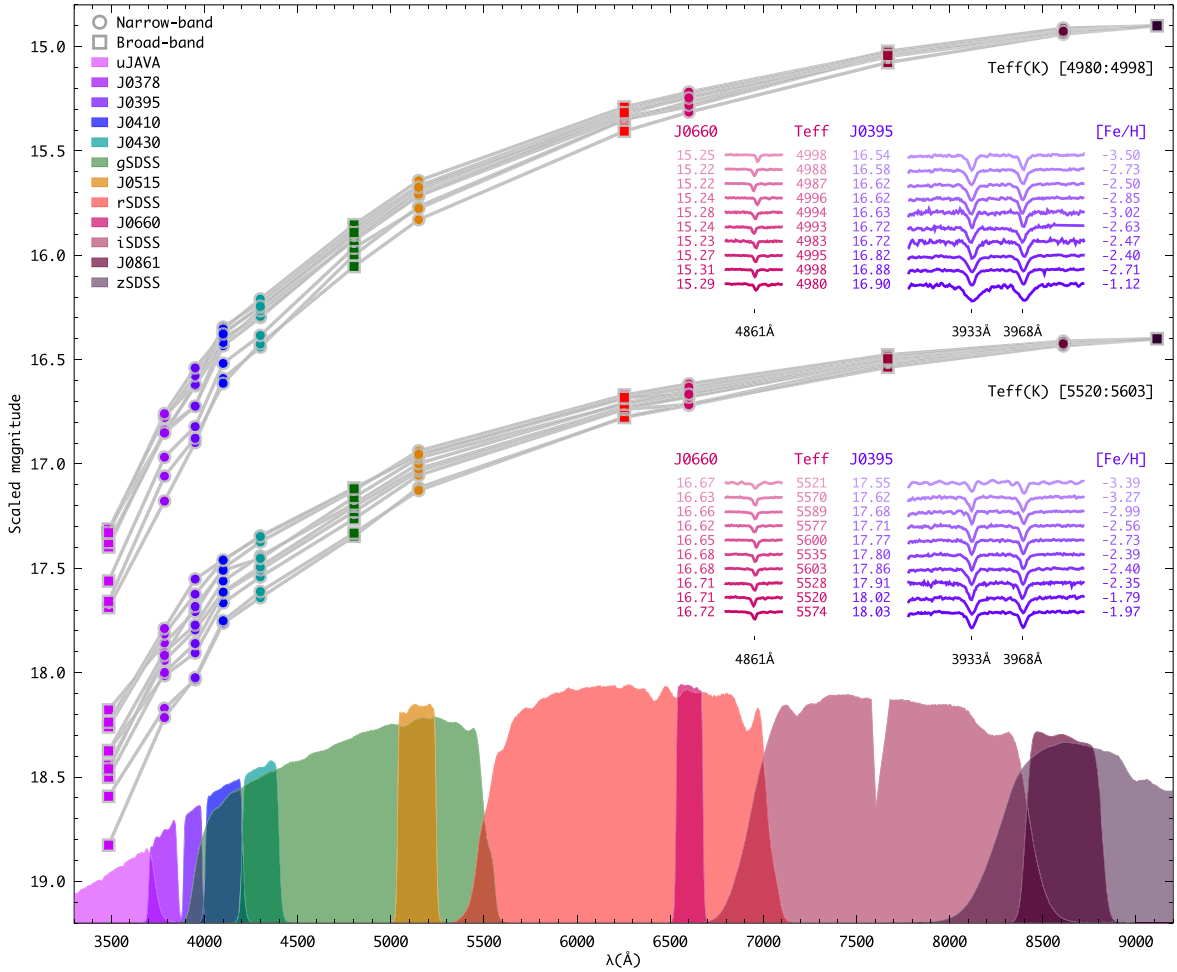

Figure 6. Spectral energy distribution (SED) for 20 selected program stars from Blanco and Gemini. Magnitudes were scaled to zSDSS = 14.9 (top) and 16.4 (bottom). The temperature range for each set is displayed right below the SEDs. The insets show the observed spectra around the Hβ and Ca II HK absorption features, sorted by their J0395 scaled magnitude. Also shown are the $T_{\rm eff}$ and [Fe/H] for each star and the S-PLUS transmission curves. See the text for further details.

0.24 dex for log g (σlog $g \in$[0.1:0.4]), 0.11 dex for [Fe/H] (σ[Fe/H] $\in$ [0.05:0.20]), and 0.21 dex for [C/Fe] and [α/Fe].

The adopted atmospheric parameters and abundance ratios for the sample are listed in Table 3. Also included in the table are the corrections for carbon abundances, based on the stellar-evolution models presented in Placco et al. (2014), the final [C/Fe], and A(C),[17] the latter two including the corrections. Figure 4 shows the log g versus $T_{\rm eff}$ diagram for the sample, compared with the YY isochrones for different metallicities (12 Gyr, 0.8 $M_\odot$, [α/Fe] = +0.4; Demarque et al. 2004). The point sizes are inversely proportional to the [Fe/H] values and typical uncertainties for log g ($\sim$0.25 dex) and $T_{\rm eff}$ ($\sim$150 K) are also shown. Based on the color selection from the S-PLUS filters, it is expected that the majority of the stars ($\sim$78%) have temperatures in the [4700:5700] K range. There is an overall agreement between observations and the isochrones for [Fe/H] = −2.0 and −3.0, apart from a small systematic offset of $\sim$50–100 K for the spectroscopic temperatures. In addition, it is evident that the majority of the higher-metallicity stars (smaller symbols, in particular [Fe/H] $\geqslant -1.0$) have $T_{\rm eff} \geqslant 5700$ K. This will be further discussed in Section 4.4.

Figure 5 shows example spectra for the 100 most metal-poor stars observed with Blanco (left panel) and Gemini South (right panel), which have both [C/Fe] and [α/Fe] determined by the n-SSPP. Also shown are the adopted parameters for each target (see Section 3 for details). The absorption features of interest for the calculation of each parameter are identified at the top of the panels. The shaded regions correspond to the specific atmospheric parameter or chemical abundance probed by the S-PLUS filters outlined at the bottom of the panels. The spectra are sorted by [Fe/H]. Despite the variation in $T_{\rm eff}$, it is possible to note the overall decrease in the strength of the Ca II features as the metallicity decreases, as well as the increase in $T_{\rm eff}$, A(C), and [α/Fe] as their associated absorption features strengthen.

4. Analysis and Discussion

4.1. [Fe/H] Sensitivity from Narrowband Photometry

As described in Section 2, the S-PLUS colors using the narrowband J0395 filter are effective in separating different metallicity regimes (see also Figure 2). Hence, for a given temperature, the difference between the J0395 and J0660 magnitudes should decrease as a function of [Fe/H].[18] An

[17] $A(\mathrm{C}) = \log(N_{\rm C}/N_{\rm H}) + 12$.

[18] As an example, for two stars with the same $T_{\rm eff}$/log g and at the same distance, the one with the lowest metallicity would be brighter in J0395.

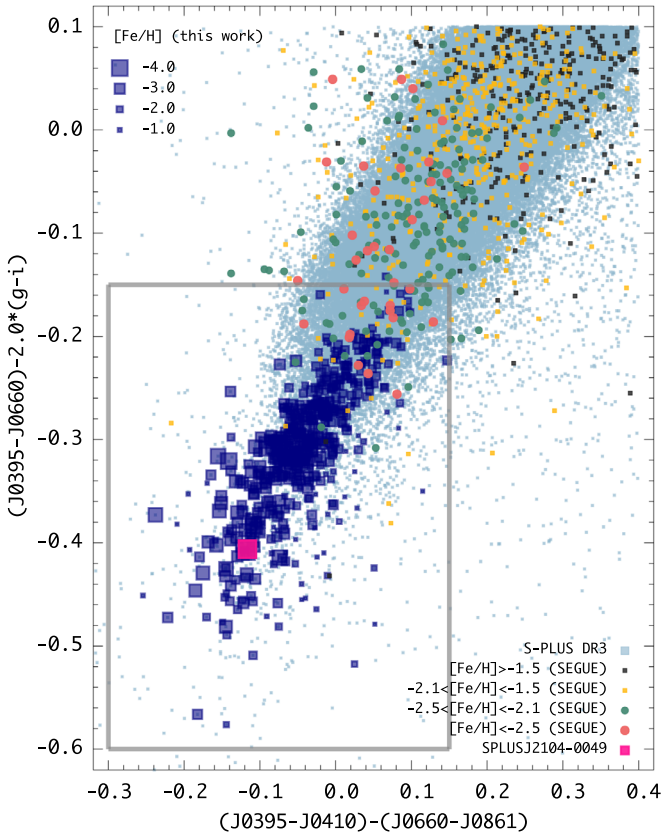

Figure 7. S-PLUS color–color diagram for S-PLUS DR3 (light blue filled squares), SDSS/SEGUE crossmatch (divided in four metallicity intervals), and the stars observed in this work (dark blue filled squares, with point sizes inversely proportional to the metallicity). The gray rectangle outlines the selection window for the spectroscopic follow-up, described in the text. Also shown is SPLUS J2104−0049, an ultra metal-poor star identified in S-PLUS by Placco et al. (2021).

attempt to illustrate and quantify this effect is shown in Figure 6. There are two sets of spectral energy distributions (SEDs) with 10 stars each, in two narrow temperature intervals. The magnitudes were scaled to an arbitrary zSDSS value in order to preserve their color indices and allow for a star-to-star comparison of the sensitivity of the other magnitudes to changes in stellar parameters. The insets show sections of the observed spectra (sorted by their J0395 scaled magnitude) around the Ca II HK and Hβ features, as well as their respective parameters ([Fe/H] and $T_{\rm eff}$) and scaled magnitudes (J0395 and J0660). Assuming that the three bluest filters carry most of the metallicity information, it is possible to qualitatively see the larger variation in magnitudes, as compared with the magnitudes from the redder filters. Under the assumption that (most) of this variation is due to changes in metallicity, it is expected that the sorted J0395 magnitudes would naturally result in a [Fe/H] sequence.

For the SEDs on the top set, all $T_{\rm eff}$ values are within 18 K, which translates into a 0.09 mag (∼0.5%) variation in the J0660 flux. As expected, there is an increase of the J0395 magnitude with [Fe/H]. The two extremes of the [Fe/H] scale have a 0.36 magnitude difference in J0395, which roughly translates into a 2.0 dex variation in [Fe/H]. At this temperature range, the above variation in the Ca II HK region flux is well above the typical magnitude uncertainties from S-PLUS, making it possible to have a good metallicity discriminant.

To a certain degree, the same applies to the bottom set of SEDs, which has an average $T_{\rm eff}$ about 500 K warmer than the top set, with a somewhat lager dispersion of 83 K. These warmer temperatures result in weaker absorption features when compared to the cooler set for a given [Fe/H], but are still larger than the typical uncertainties in the measured flux. For this group, the variation in the J0660 magnitude is very small (0.05 mag), while the difference between the extremes in J0395 (0.48 mag) still translates into a 1.5 dex range in terms of [Fe/H].

4.2. Effectiveness of S-PLUS Color Selection

One of the main goals of this work is to improve the success rate of finding low-metallicity stars from photometry, taking advantage of the metallicity sensitivity of the S-PLUS narrowband filters. Figure 7 shows the color–color diagram for the S-PLUS DR3 data, the crossmatch between S-PLUS and SDSS/SEGUE (color-coded by metallicity range), and the 522 stars observed in this work. The point size is inversely proportional to [Fe/H]. The gray rectangle outlines the selection window for the spectroscopic follow-up, as defined in Section 2: (J0395−J0410)−(J0660−J0861) ∈[−0.30:0.15] and (J0395−J0660)−2×(g−i) ∈[−0.60:−0.15]. Also shown in the figure is SPLUS J2104−0049, the first ultra metal-poor star identified in S-PLUS, with [Fe/H] = −4.03[19] (Placco et al. 2021).

There is, as expected, a strong correlation between metallicity and the position of a star in this color–color diagram. However, that does not imply a direct translation between these colors and [Fe/H], as evidenced by the stars with smaller points (higher metallicities) present toward negative colors. However, these higher-metallicity stars can be filtered out by another color combination (see Section 4.4 below for further details). What still holds true, as set forth by Figure 2, is the fact that the *fraction* of stars with [Fe/H] ⩽ −2.0 increases for decreasing (J0395−J0660)−2×(g−i) and (J0395−J0410)−(J0660−J0861).

A different procedure to assess the efficiency of the color selection is by looking at the MDF of the observed stars and compare it with previous attempts of following up low-metallicity star candidates. The top panel of Figure 8 shows the MDF of the stars observed in this work, compared with data from Placco et al. (2018, 2019) and Limberg et al. (2021b) [20] in the middle panels. The total number of stars and fractions for different metallicity ranges are also shown for each sample. The bottom panel shows the cumulative distribution function (CDF) for the three samples, indicating the 80th percentile value for [Fe/H]. It is possible to see that the S-PLUS color selection is far superior than the previous efforts in selecting low-metallicity star candidates. The success rate for [Fe/H] ⩽ −2.0 is 83^{+3}_{-3}%,[21] as compared to 60% in Placco et al. (2018), 39% in Placco et al. (2019), and 30% in Limberg et al. (2021b). Finally, the fraction of stars with [Fe/H] ⩽ −3.0 (15%) is higher than the fraction of stars with [Fe/H] > −1.5 (11%), which confirms the effectiveness of the S-PLUS color window in selecting low-metallicity stars.

[19] The n-SSPP estimated [Fe/H] = −4.29 from the Gemini/GMOS medium-resolution spectrum.

[20] Even though these three efforts have followed-up data selected from different approaches, both had the goal of maximizing the number of observed stars with [Fe/H] ⩽ −2.0. A comparison could also be made with the work of Aguado et al. (2019), Da Costa et al. (2019), and Galarza et al. (2022). However, these studies used photometric metallicities for their target selection, as opposed to the color–color diagrams employed by this work.

[21] Uncertainties in the fractions are represented by the Wilson score confidence intervals (Wilson 1927).

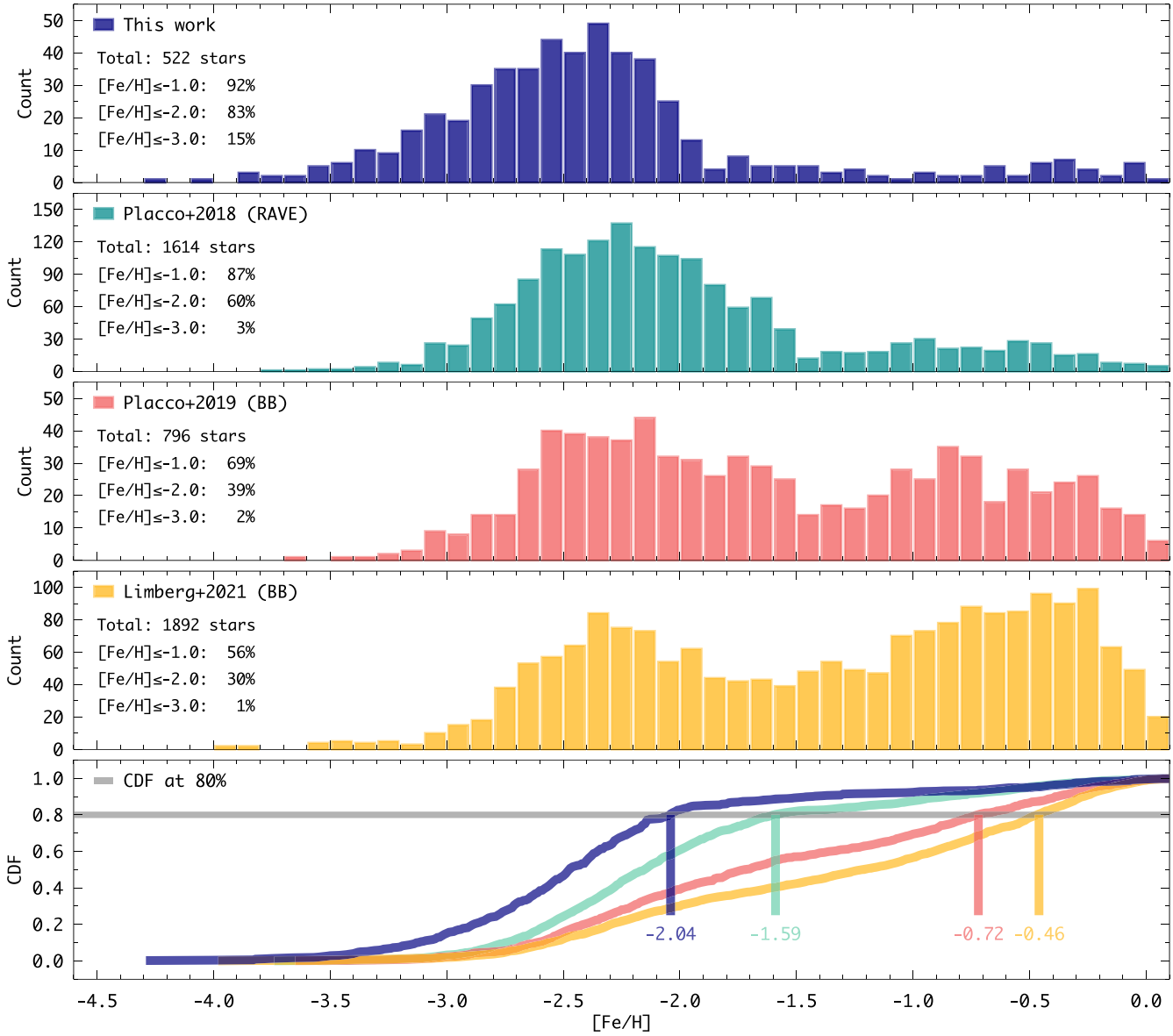

Figure 8. Metallicity histogram for the program stars (top panel), compared with the distributions from Placco et al. (2018, 2019) and Limberg et al. (2021b) (middle panels). Each panel shows the total number of stars and the fractions for different metallicity regimes. The bottom panel shows the cumulative distribution functions (CDFs) for the three samples, marking the [Fe/H] value for which they reach 80%.

4.3. Carbon and α-element Abundances

The carbon and α-element abundances calculated by the n-SSPP can provide further insight on the origin of the observed stars and serve as selection criteria for high-resolution spectroscopic follow-up. Even though the carbon abundances in the SEGUE sample were not used for the target selection in this work, the (g−i) color (and, to some extent, also the J0395 and J0410 magnitudes) can be affected by the presence of carbon molecular bands in the spectrum. As a consequence of the decreased emerging flux on the g band, a fraction of cool carbon-enhanced stars may fall outside the (g−i) [22] window defined in Section 2. Regardless, the abundances measured for the program stars allow for the calculation of the fractions of carbon-enhanced metal-poor (CEMP, $[C/Fe] \geqslant +0.7$; Aoki et al. 2007) stars as a function of the metallicity.

Figure 9 shows the distribution of A(C) (left panel) and $[\alpha/Fe]$ (right panel) for the sample stars as a function of the metallicity. The auxiliary panels show the marginal distributions. The bottom left panel shows both the differential and cumulative CEMP fractions. Solid lines mark the solar values for the quantities, as well as the CEMP definition on the left panel and the average $[\alpha/Fe] = +0.4$ for the Galactic halo (Venn et al. 2004; Kobayashi et al. 2006) in the right panel. The point sizes are proportional to the temperature. The CEMP groups labeled are loosely defined based on the arguments presented in Yoon et al. (2016), which were built upon the work of Spite et al. (2013), Bonifacio et al. (2015), and Hansen et al. (2015). The average α-element abundance for the sample ($[\alpha/Fe] = +0.29$) is somewhat lower than the typical value for stars with $[Fe/H] < -2.0$ and there is no apparent trend with metallicities.

Stars in the CEMP Group I are believed to have acquired their carbon in a binary system from a now-evolved companion

[22] As an example, the star SDSS J1327+3335, with $T_{\rm eff} = 4530$ K, $[Fe/H] = -3.38$, and $[C/Fe] = +2.18$, has (g−i) = 1.718 (Yoon et al. 2020).

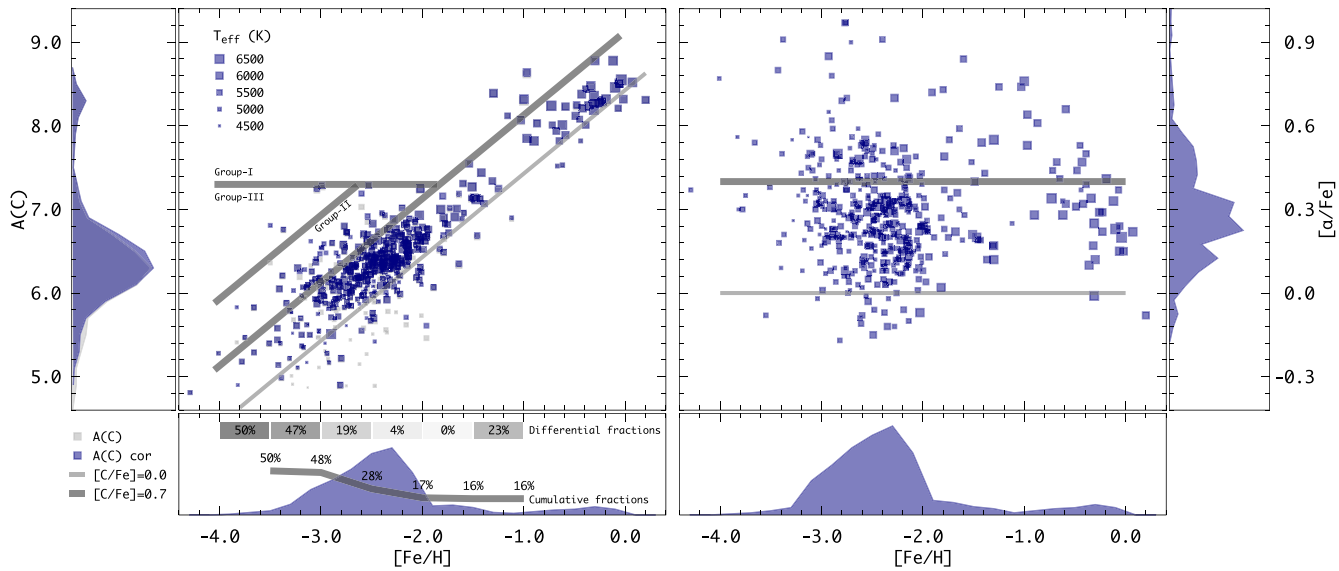

Figure 9. Absolute carbon, (A(C), corrected as described in the text; left panel), and α-element abundance ratios, [α/Fe] (right panel), as a function of the metallicity calculated by the n-SSPP. The side and bottom panels show the marginal distributions. The solid line in the bottom left panel shows the cumulative CEMP fractions for the stars with $-3.5 \leqslant$ [Fe/H] $\leqslant -1.0$ and the numbers on the top part of the panel are the differential fractions for 0.5 dex [Fe/H] bins. Point sizes are proportional to $T_{\rm eff}$.

that went through its asymptotic giant branch phase (extrinsic enrichment; Placco et al. 2014). Members of Groups II and III, on the other hand, carry in their atmosphere the carbon signature inherited from its parent population (intrinsic enrichment; Placco et al. 2014). The distinction between Groups II and III lies on specific characteristics of the massive stars that polluted the gas clouds from which the subsequent low-mass stars were formed. For the sample presented in this work, there are 68 CEMP stars, with 4 stars in Group I, 60 in Group II, and 4 in Group III. Compared with the work of Yoon et al. (2016), the sample presented in this work has an exceptionally low number of Group I stars, which should be the majority in the CEMP population. This may be partially[23] a consequence of the (g−i) restriction mentioned above and other S-PLUS color selections, which would exclude most of the higher-metallicity and higher-carbon-abundance stars associated with Group I.

The cumulative CEMP fractions shown in the lower panel of Figure 9 are consistently lower for [Fe/H] < -1.0 and < -2.0 when compared to other empirical estimates in the literature, derived from samples with similar spectral resolution (Placco et al. 2018; Yoon et al. 2018; Placco et al. 2019; Limberg et al. 2021b). This may be, once more, a consequence of the selection methods employed in this work. The same applies to the differential fractions. The fractions are in better agreement for the [Fe/H] < -3.0 regime, which could be due to the fact that Group III stars dominate the CEMP population in this metallicity regime (see Arentsen et al. 2022 for a complete review of the CEMP fractions in the literature).

4.4. Further Improvements in the Color Selection

Even though the S-PLUS color selections presented in this work are effective in selecting low-metallicity stars, additional restrictions can be made in order to decrease the number of stars with [Fe/H] $\geqslant -1.0$ for further spectroscopic follow-up and targeting. Further inspection of Figure 4 reveals that 42% of the stars with $T_{\rm eff} \geqslant 5900$ K have [Fe/H] $\geqslant -1.0$, while only 3% of the stars with $T_{\rm eff} < 5900$ K have [Fe/H] $\geqslant -1.0$.

An exploratory analysis was conducted to search for an additional S-PLUS color combination that would help remove the higher-metallicity stars for the continuation of the spectroscopic follow-up. One such candidate is (J0378−i)−(J0410−J0660), which contains the metallicity-sensitive J0378 filter and the temperature-sensitive (J0410−J0660) color index. The top panel of Figure 10 shows the behavior of this color as a function of the metallicity. It is possible to see a very strong correlation between the two quantities, and a tentative cut was made at (J0378−i)−(J0410−J0660) =0.80. The high color index subsample (red points) is dominated by the higher-metallicity stars, with only 30% of the stars with [Fe/H] $\leqslant -1.0$ and 39% with [Fe/H] $\leqslant -2.0$. For the low color index subsample (blue points), the fractions are 98% for stars with [Fe/H] $\leqslant -1.0$ and 88% with [Fe/H] $\leqslant -2.0$. The bottom panel shows the CDFs for both subsamples, indicating the 80th percentile value for [Fe/H].

This additional color restriction further improves the success rate for the identification of stars with [Fe/H] $\leqslant -2.0$ from the S-PLUS photometry. Even though there are low-metallicity stars with (J0378−i)−(J0410−J0660) > 0.8, their fraction is substantially smaller than for (J0378−i)−(J0410−J0660) < 0.8. The stars at the high color index subsample with [Fe/H] $\leqslant -2.0$ are all low temperature ($T_{\rm eff} \lesssim 4800$ K) and low carbon ([C/Fe] $\leqslant 0.0$).

5. Conclusions

This work presented the medium-resolution spectroscopic follow-up of 522 low-metallicity star candidates selected from their S-PLUS photometry. By using metallicity-sensitive colors, the success rate found is 92^{+2}_{-3}% for [Fe/H] $\leqslant -1.0$, 83^{+3}_{-3}% for [Fe/H] $\leqslant -2.0$, and 15^{+3}_{-3}% for [Fe/H] $\leqslant -3.0$, including two ultra metal-poor stars ([Fe/H] $\leqslant -4.0$). Based on the carbonicity determinations, there are 68 CEMP stars in the

[23] Arentsen et al. (2022) point out that, in general, low-metallicity star samples from medium-resolution spectroscopy show a lower than expected fraction of CEMP Group I stars when compared to high-resolution samples.

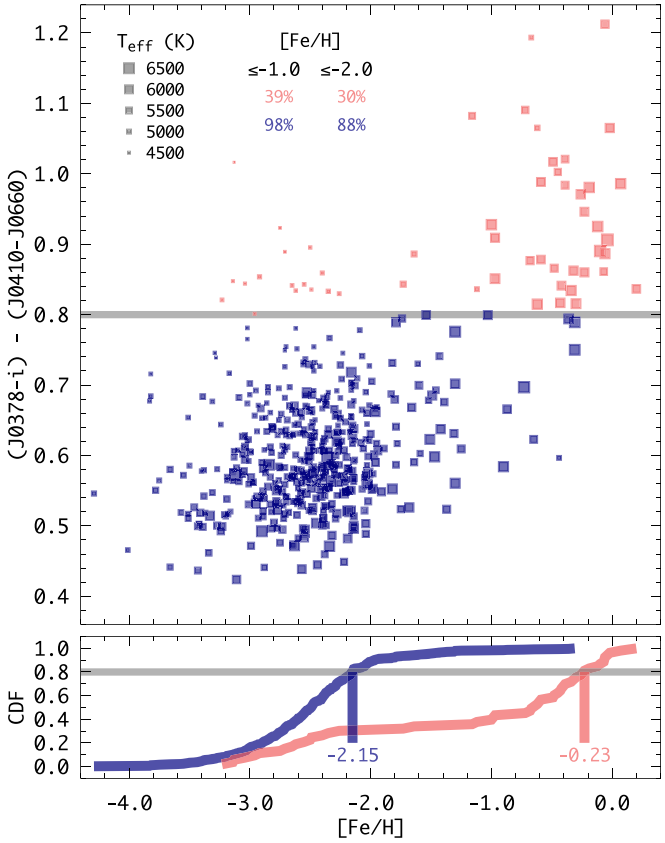

Figure 10. Top panel: (J0378−i) − (J0410−J0660) as a function of the metallicity for the observed sample, with the gray line marking the proposed color cut. Also shown are the fractions of stars with [Fe/H] $\leqslant -1.0$ and $\leqslant -2.0$ for the two subsamples. The point sizes are proportional to $T_{\rm eff}$. Bottom panel: cumulative distribution functions (CDFs) for the two subsamples, marking the [Fe/H] value for which they reach 80%.

sample, including 60 Group II and 4 Group III. Most of these are already being followed up with high-resolution spectroscopy in order to determine their chemical abundance pattern and further understand their origin. Based on the [Fe/H] determined in this work, a further color restriction is proposed, which can potentially increase the fractions of stars with [Fe/H] $\leqslant -1.0$ and $\leqslant -2.0$ to 98% and 88%, respectively.

The unpretentious color selection described in this work is not only extremely effective in providing targets for further spectroscopic studies, but also establishes a framework in which upcoming fiber-fed multiplex surveys can benefit from in terms of targeting. These surveys will continue to provide the individual pieces that constitute the cosmic puzzle that is the chemical evolution of the universe.

The authors would like to thank the anonymous referee and members of the S-PLUS community (Guilherme Limberg, Leandro Beraldo e Silva, and Simone Daflon) who provided insightful comments on the manuscript. The work of V.M.P. is supported by NOIRLab, which is managed by the Association of Universities for Research in Astronomy (AURA) under a cooperative agreement with the National Science Foundation. F.A.-F. acknowledges funding for this work from FAPESP grants 2018/20977-2 and 2021/09468-1. A.A. gratefully acknowledges funding from the European Research Council (ERC) under the European Union's Horizon 2020 research and innovation program (grant agreement No. 834148). Y.S.L. acknowledges support from the National Research Foundation (NRF) of Korea grant funded by the Ministry of Science and ICT (NRF-2021R1A2C1008679). The S-PLUS project, including the T80-South robotic telescope and the S-PLUS scientific survey, was founded as a partnership between the Fundação de Amparo à Pesquisa do Estado de São Paulo (FAPESP), the Observatório Nacional (ON), the Federal University of Sergipe (UFS), and the Federal University of Santa Catarina (UFSC), with important financial and practical contributions from other collaborating institutes in Brazil, Chile (Universidad de La Serena), and Spain (Centro de Estudios de Física del Cosmos de Aragón, CEFCA). We further acknowledge financial support from the São Paulo Research Foundation (FAPESP), the Brazilian National Research Council (CNPq), the Coordination for the Improvement of Higher Education Personnel (CAPES), the Carlos Chagas Filho Rio de Janeiro State Research Foundation (FAPERJ), and the Brazilian Innovation Agency (FINEP). The members of the S-PLUS collaboration are grateful for the contributions from CTIO staff in helping in the construction, commissioning and maintenance of the T80-South telescope and camera. We are also indebted to Rene Laporte, INPE, and Keith Taylor for their important contributions to the project. From CEFCA, we thank Antonio Marín-Franch for his invaluable contributions in the early phases of the project, David Cristóbal-Hornillos and his team for their help with the installation of the data reduction package JYPE version 0.9.9, César Íñiguez for providing 2D measurements of the filter transmissions, and all other staff members for their support with various aspects of the project. Based on observations made at Cerro Tololo Inter-American Observatory at NSF's NOIRLab (NOIRLab Prop. IDs 2019B-0069, 2020A-0032, 2022A-210002; PI: V. Placco), which is managed by the Association of Universities for Research in Astronomy (AURA) under a cooperative agreement with the National Science Foundation. Based on observations obtained at the international Gemini Observatory (Program IDs: GS-2019A-Q-408, GS-2021A-Q-419, GS-2022A-Q-406), a program of NSF's NOIRLab, which is managed by the Association of Universities for Research in Astronomy (AURA) under a cooperative agreement with the National Science Foundation. on behalf of the Gemini Observatory partnership: the National Science Foundation (United States), National Research Council (Canada), Agencia Nacional de Investigación y Desarrollo (Chile), Ministerio de Ciencia, Tecnología e Innovación (Argentina), Ministério da Ciência, Tecnologia, Inovações e Comunicações (Brazil), and Korea Astronomy and Space Science Institute (Republic of Korea). This research has made use of NASA's Astrophysics Data System Bibliographic Services; the arXiv preprint server operated by Cornell University; the SIMBAD database hosted by the Strasbourg Astronomical Data Center; and the online Q&A platform stackoverflow (http://stackoverflow.com/).

Facilities: Blanco (COSMOS), Gemini:South (GMOS).

Software: awk (Aho et al. 1987), dustmaps (Green 2018), DRAGONS (Labrie et al. 2019), gnuplot (Williams & Kelley 2015), IRAF (Tody 1986, 1993), matplotlib (Hunter 2007), n-SSPP (Beers et al. 2014), numpy (Harris et al. 2020), pandas (McKinney 2010), sed (Mcmahon 1979), stilts (Taylor 2006).

ORCID iDs

Vinicius M. Placco https://orcid.org/0000-0003-4479-1265
Felipe Almeida-Fernandes https://orcid.org/0000-0002-8048-8717

Anke Arentsen https://orcid.org/0000-0002-0544-2217
Young Sun Lee https://orcid.org/0000-0001-5297-4518
William Schoenell https://orcid.org/0000-0002-4064-7234
Tiago Ribeiro https://orcid.org/0000-0002-0138-1365
Antonio Kanaan https://orcid.org/0000-0002-2484-7551

References

Aguado, D. S., Youakim, K., González Hernández, J. I., et al. 2019, MNRAS, 490, 2241
Aho, A. V., Kernighan, B. W., & Weinberger, P. J. 1987, The AWK Programming Language (Boston, MA: Addison-Wesley Longman)
Allende Prieto, C. 2016, A&A, 595, A129
Almeida-Fernandes, F., SamPedro, L., Herpich, F. R., et al. 2022, MNRAS, 511, 4590
Alonso, A., Arribas, S., & Martinez-Roger, C. 1996, A&A, 313, 873
Alonso, A., Arribas, S., & Martínez-Roger, C. 1999, A&AS, 140, 261
An, D., Beers, T. C., Santucci, R. M., et al. 2015, ApJL, 813, L28
An, D., Beers, T. C., Johnson, J. A., et al. 2013, ApJ, 763, 65
Aoki, W., Beers, T. C., Christlieb, N., et al. 2007, ApJ, 655, 492
Arentsen, A., Placco, V. M., Lee, Y. S., et al. 2022, MNRAS, in press
Beers, T. C., & Christlieb, N. 2005, ARA&A, 43, 531
Beers, T. C., Norris, J. E., Placco, V. M., et al. 2014, ApJ, 794, 58
Beers, T. C., Placco, V. M., Carollo, D., et al. 2017, ApJ, 835, 81
Bessell, M., Bloxham, G., Schmidt, B., et al. 2011, PASP, 123, 789
Bessell, M. S. 1979, PASP, 91, 589
Bonifacio, P., Monai, S., & Beers, T. C. 2000, AJ, 120, 2065
Bonifacio, P., Caffau, E., Spite, M., et al. 2015, A&A, 579, A28
Bromm, V., & Larson, R. B. 2004, ARA&A, 42, 79
Carney, B. W., & Peterson, R. C. 1981, ApJ, 245, 238
Casagrande, L., Ramírez, I., Meléndez, J., Bessell, M., & Asplund, M. 2010, A&A, 512, A54
Casagrande, L., Wolf, C., Mackey, A. D., et al. 2019, MNRAS, 482, 2770
Cenarro, A. J., Moles, M., Cristóbal-Hornillos, D., et al. 2019, A&A, 622, A176
Chiti, A., Frebel, A., Mardini, M. K., et al. 2021a, ApJS, 254, 31
Chiti, A., Mardini, M. K., Frebel, A., & Daniel, T. 2021b, ApJL, 911, L23
Cordoni, G., Da Costa, G. S., Yong, D., et al. 2021, MNRAS, 503, 2539
Da Costa, G. S., Bessell, M. S., Mackey, A. D., et al. 2019, MNRAS, 489, 5900
Davies, R. L., Allington-Smith, J. R., Bettess, P., et al. 1997, Proc. SPIE, 2871, 1099
Demarque, P., Woo, J.-H., Kim, Y.-C., & Yi, S. K. 2004, ApJS, 155, 667
Dotter, A., Chaboyer, B., Jevremović, D., et al. 2008, ApJS, 178, 89
Frebel, A., & Norris, J. E. 2015, ARA&A, 53, 631
Fukugita, M., Ichikawa, T., Gunn, J. E., et al. 1996, AJ, 111, 1748
Galarza, C. A., Daflon, S., Placco, V. M., et al. 2022, A&A, 657, A35
Gimeno, G., Roth, K., Chiboucas, K., et al. 2016, Proc. SPIE, 9908, 99082S
Greaves, W. M. H., Davidson, C., & Martin, E. 1929, MNRAS, 90, 104
Green, G. 2018, JOSS, 3, 695
Gustafsson, B., Edvardsson, B., Eriksson, K., et al. 2008, A&A, 486, 951
Hansen, T., Hansen, C. J., Christlieb, N., et al. 2015, ApJ, 807, 173
Harris, C. R., Millman, K. J., van der Walt, S. J., et al. 2020, Natur, 585, 357
Heger, A., & Woosley, S. E. 2002, ApJ, 567, 532
Huang, Y., Chen, B. Q., Yuan, H. B., et al. 2019, ApJS, 243, 7
Hunter, J. D. 2007, CSE, 9, 90
Ivezić, Ž., Beers, T. C., & Jurić, M. 2012, ARA&A, 50, 251
Ivezić, Ž., Sesar, B., Jurić, M., et al. 2008, ApJ, 684, 287
Keller, S. C., Schmidt, B. P., Bessell, M. S., et al. 2007, PASA, 24, 1
Kobayashi, C., Umeda, H., Nomoto, K., Tominaga, N., & Ohkubo, T. 2006, ApJ, 653, 1145
Labrie, K., Anderson, K., Cárdenes, R., Simpson, C., & Turner, J. E. H. 2019, in ASP Conf. Ser. 523, Astronomical Data Analysis Software and Systems XXVII, ed. P. J. Teuben (San Francisco, CA: ASP), 321
Lee, Y. S., Beers, T. C., Sivarani, T., et al. 2008a, AJ, 136, 2022
Lee, Y. S., Beers, T. C., Sivarani, T., et al. 2008b, AJ, 136, 2050
Lee, Y. S., Beers, T. C., Allende Prieto, C., et al. 2011, AJ, 141, 90
Lee, Y. S., Beers, T. C., Masseron, T., et al. 2013, AJ, 146, 132
Leggett, S. K., Burningham, B., Saumon, D., et al. 2010, ApJ, 710, 1627
Limberg, G., Rossi, S., Beers, T. C., et al. 2021a, ApJ, 907, 10
Limberg, G., Santucci, R. M., Rossi, S., et al. 2021b, ApJ, 913, 11
Lucatello, S., Beers, T. C., Christlieb, N., et al. 2006, ApJL, 652, L37
Majewski, S. R., Ostheimer, J. C., Kunkel, W. E., & Patterson, R. J. 2000, AJ, 120, 2550
Martini, P., Elias, J., Points, S., et al. 2014, Proc. SPIE, 9147, 91470Z
Masseron, T., Johnson, J. A., Plez, B., et al. 2010, A&A, 509, A93
Masseron, T., Plez, B., Van Eck, S., et al. 2014, A&A, 571, A47
McKinney, W. 2010, in Proc. of the 9th Python in Science Conf., ed. S. van der Walt & J. Millman, 56
Mcmahon, L. E. 1979, UNIX Programmer's Manual, Vol. 2 (7th ed.; Bell Telephone Laboratories: Murray Hill, NJ)
Mendes de Oliveira, C., Ribeiro, T., Schoenell, W., et al. 2019, MNRAS, 489, 241
Meynet, G., Ekström, S., & Maeder, A. 2006, A&A, 447, 623
Molino, A., Costa-Duarte, M. V., Sampedro, L., et al. 2020, MNRAS, 499, 3884
Norris, J. E., Bessell, M. S., Yong, D., et al. 2013, ApJ, 762, 25
Placco, V. M., Frebel, A., Beers, T. C., & Stancliffe, R. J. 2014, ApJ, 797, 21
Placco, V. M., Beers, T. C., Santucci, R. M., et al. 2018, AJ, 155, 256
Placco, V. M., Santucci, R. M., Beers, T. C., et al. 2019, ApJ, 870, 122
Placco, V. M., Roederer, I. U., Lee, Y. S., et al. 2021, ApJL, 912, L32
Plez, B. 2012, Turbospectrum: Code for Spectral Synthesis, Astrophysics Source Code Library, ascl:1205.004
Rockosi, C. M., Lee, Y. S., Morrison, H. L., et al. 2022, ApJS, 259, 60
Schlegel, D. J., Finkbeiner, D. P., & Davis, M. 1998, ApJ, 500, 525
Schuster, W. J., & Nissen, P. E. 1989, A&A, 221, 65
Shank, D., Beers, T. C., Placco, V. M., et al. 2022, ApJ, 926, 26
Spite, M., Caffau, E., Bonifacio, P., et al. 2013, A&A, 552, A107
Starkenburg, E., Martin, N., Youakim, K., et al. 2017, MNRAS, 471, 2587
Steinmetz, M., Guiglion, G., McMillan, P. J., et al. 2020, AJ, 160, 83
Taylor, M. B. 2006, in ASP Conf. Ser. 351, Astronomical Data Analysis Software and Systems XV, ed. C. Gabriel (San Francisco, CA: ASP), 666
Tody, D. 1986, Proc. SPIE, 627, 733
Tody, D. 1993, in ASP Conf. Ser. 52, Astronomical Data Analysis Software and Systems II, ed. R. J. Hanisch, R. J. V. Brissenden, & J. Barnes (San Francisco, CA: ASP), 173
Venn, K. A., Irwin, M., Shetrone, M. D., et al. 2004, AJ, 128, 1177
Wallerstein, G. 1964, PASP, 76, 175
Whitten, D. D., Placco, V. M., Beers, T. C., et al. 2019, A&A, 622, A182
Whitten, D. D., Placco, V. M., Beers, T. C., et al. 2021, ApJ, 912, 147
Williams, T., & Kelley, C. 2015, Gnuplot 5.0: An Interactive Plotting Program, http://www.gnuplot.info/
Wilson, E. B. 1927, J. Am. Stat. Assoc., 22, 209
Wolf, C., Onken, C. A., Luvaul, L. C., et al. 2018, PASA, 35, e010
Woosley, S. E., & Weaver, T. A. 1995, ApJS, 101, 181
Yanny, B., Rockosi, C., Newberg, H. J., et al. 2009, AJ, 137, 4377
Yoon, J., Whitten, D. D., Beers, T. C., et al. 2020, ApJ, 894, 7
Yoon, J., Beers, T. C., Placco, V. M., et al. 2016, ApJ, 833, 20
Yoon, J., Beers, T. C., Dietz, S., et al. 2018, ApJ, 861, 146
York, D. G., Adelman, J., Anderson, J. E., Jr., et al. 2000, AJ, 120, 1579
Youakim, K., Starkenburg, E., Aguado, D. S., et al. 2017, MNRAS, 472, 2963
Yuan, Z., Myeong, G. C., Beers, T. C., et al. 2020, ApJ, 891, 39